JOURNAL OF GEOPHYSICAL RESEARCH, VOL. 101, NO. C2, PAGES 3561–3572, FEBRUARY 15, 1996

Comparison of field observations of the vertical distribution of suspended sand and its prediction by models

T. H. Lee
Daewoo Corporation, Seoul

D. M. Hanes
Coastal and Oceanographic Engineering Department, University of Florida, Gainesville

Abstract. Models for the vertical distribution of suspended sediment under waves and currents are compared with field observations. The models include a diffusion-based model, a convection-based model, and a combined convection-diffusion model. The field observations were carried out at Vilano Beach, Florida, in a water depth of approximately 3 to 4 m, with a median grain diameter of 0.14 mm. The rms wave height ranged from approximately 0.4 to 1.2 m. Under low waves the seabed was covered with very small ripples, and under the higher waves, sheet flow conditions were present. The diffusion-based model was found to best describe the observed data under high wave conditions, but the convection model was more accurate under low wave conditions. Over all conditions the combined model was the most accurate. These results are consistent with the different mechanisms for mixing suspended sediment over flat versus rippled beds.

Introduction

The suspension of sediment by waves and currents involves a series of processes by which sediment particles in the bed or very near the bed are entrained and transported up to higher levels by hydrodynamic forces [*Bagnold*, 1956]. A steady vertical distribution of particles in suspension is mainly the result of the balance between a net upward sediment flux resulting from hydrodynamic forces and downward settling of particles due to gravity. The upward sediment flux occurs on a variety of temporal and spatial scales. The dominant scales are determined by the flow conditions, the characteristics of the sediment, and the bottom topography.

Many models for sediment transport employ gradient diffusion models to describe sediment flux by turbulent mixing. As a recent example, *Wikramanayake* [1993] suggested a suspended sediment model using a three-layer, time-invariant eddy viscosity, modified from *Grant and Madsen* [1979]. As an example of an alternative to gradient diffusion models, *Nielsen* [1992] suggested a convection model which incorporated coherent, structured motions of sediment. A good example of this type of structure is the dense sediment cloud found in vortices above a rippled bed. Nielsen also suggested a combined convection-diffusion model with a time-invariant, vertically uniform, eddy diffusivity profile to accommodate sediment mixing on both small and large scales.

In the present study the mechanisms of sediment suspension under combined wave-current conditions are reviewed. We then review a pure diffusion model and a pure convection model for sand suspension under waves and currents. A combined convection-diffusion model is developed using a time-invariant, vertically varying eddy diffusivity profile, along with a probability distribution function of sediment entrainment. All of the models are then compared to measured field data.

Paper number 95JC03283.
0148-0227/96/95JC-03283$05.00

Review of Models

The time rate of change of the suspended sediment concentration at a certain elevation is given by the following conservation equation, assuming that the horizontal gradients are negligible relative to the vertical gradients

$$\frac{\partial C(z)}{\partial t} = w_0 \frac{\partial C(z)}{\partial z} - \frac{\partial q_u(z)}{\partial z} \tag{1}$$

In (1), $C(z)$ is the instantaneous concentration of the suspended sediment, w_0 is settling velocity of the sediment particles, and q_u is the upward flux of the sediment. In a diffusion model the upward transport q_u is typically assumed proportional to the concentration gradient, where ε_s is the eddy diffusivity.

$$q_u = -\varepsilon_s \frac{\partial C}{\partial z} \tag{2}$$

By substituting (2) into (1), taking the time average, integrating, and applying the boundary condition that the sediment concentration and its flux vanish at infinity, the following equation is obtained, where the overbar indicates the time mean:

$$w_0 \bar{C} + \varepsilon_s \frac{d\bar{C}}{dz} = 0 \tag{3}$$

Wikramanayake [1993] suggested a three-layer diffusion model in which the time-invariant eddy viscosity model of *Grant and Madsen* [1979] is somewhat modified. The profile of the eddy diffusivity is expressed by the following equation:

$$\varepsilon_s = \begin{cases} \kappa u_{*cw} z, & 0 \le z \le \alpha\delta \\ \kappa u_{*cw} \alpha\delta & \alpha\delta \le z \le \alpha\delta/\varepsilon \\ \kappa u_{*c} z, & \alpha\delta/\varepsilon \le z \end{cases} \tag{4}$$

where u_{*cw} is the combined wave-current friction velocity, u_{*c} is current friction velocity, ε is u_{*c}/u_{*cw}, and δ is $\kappa u_{*cw}/\omega$, in which κ and ω are the von Karman constant and the wave

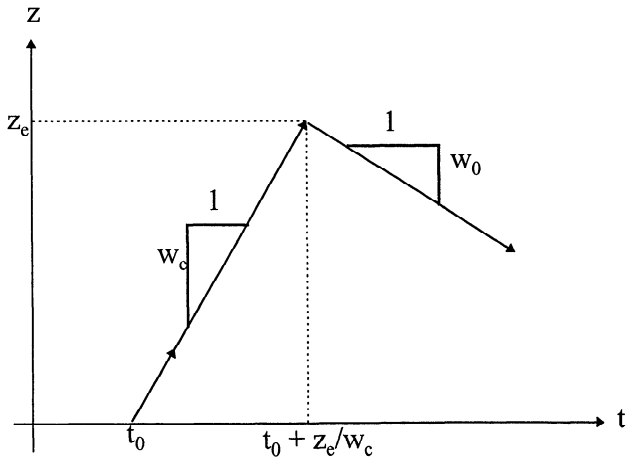

Figure 1. Motion of a particle in convective process [from *Nielsen*, 1992].

frequency, respectively. The suggested value of the experimental free parameter α is 0.5. By substituting (4) into (3), *Wikramanayake* [1993] obtained the following expression for the vertical distribution of suspended sediment concentration:

$$\frac{\bar{C}(\zeta)}{\bar{C}_r}=\begin{cases}\left[\dfrac{\zeta}{\zeta_r}\right]^{-a}, & \zeta_r \le \zeta < \alpha \\ \left[\dfrac{\alpha}{\zeta_r e}\right]^{-a} \exp\left(-\dfrac{a\zeta}{\alpha}\right), & \alpha \le \zeta < \alpha/\varepsilon \\ \left[\dfrac{\alpha}{\zeta_r e}\right]^{-a}\left[\dfrac{e\varepsilon}{\alpha}\zeta\right]^{-a/\varepsilon}, & \alpha/\varepsilon \le \zeta\end{cases} \tag{5}$$

where ζ is z/δ, a is $w_0/\kappa u_{*cw}$, e is exp (1), and C_r is the concentration at a reference level $\zeta = \zeta_r$.

Nielsen [1992] described the convective mixing quantitatively with the simple model illustrated in Figure 1. At the beginning of the convective process a sand particle is picked up from the bed at time $t = t_0$. The sand particle travels upward in a cloud with speed w_c. As the cloud moves up, it exchanges sand and water with its surroundings, and the exchanged particles are said to reach their entrainment level z_e. After reaching its entrainment level at time $t_0 + z_e/w_c$, the sand particle is assumed to settle out with its still water settling velocity w_0.

Nielsen [1992] suggested the following expression for the convective upward sediment flux:

$$q_u(z, t) = P\left(t - \frac{z}{w_c}\right) F(z) \tag{6}$$

where $P(t)$ is a nonnegative function describing the instantaneous pickup rate at the bed, w_c is the average vertical convection velocity, and $F(z)$ is the mass of sediment above a certain elevation z, normalized by its value at the bed. By substituting (6) into (1) and integrating with respect to z, Nielsen obtained the following expression:

$$w_0\bar{C}(z) = \bar{P}F(z) \tag{7}$$

By applying the stationary bed boundary condition and using $F(0) = 1$ for pure convection, we get the following equation:

$$w_0\bar{C}(0) - \bar{P} = 0 \tag{8}$$

Finally, the vertical distribution of the time-averaged suspended concentration is

$$\frac{\bar{C}(z)}{\bar{C}(0)} = F(z) \tag{9}$$

Nielsen [1992] also suggested the following entrainment probability distribution based upon laboratory observation over rippled beds by *McFetridge and Nielsen* [1985] and the study on the oscillatory boundary layer by *Nielsen* [1984]:

$$F(z) = \left(1 + \frac{z}{0.09\sqrt{k_b A_b}}\right)^{-2} \tag{10}$$

where k_b and A_b are the equivalent Nikuradse roughness and the horizontal semiexcursion of the orbital motion near the bed, respectively.

Combined Convection-Diffusion Model

The pure convection model and the pure diffusion model are combined to accommodate a variety of vertical mixing scales. This model is similar to the combined model of *Nielsen* [1992], except that we utilize the eddy viscosity model of *Wikramanayake* [1993] to characterize the diffusion process. In the combined model the upward transport of the suspended sediment is described by the sum of the diffusive flux and the convective flux,

$$q_u(z, t) = -\varepsilon_s \frac{\partial C}{\partial z} + P\left(t - \frac{z}{w_c}\right) F(z) \tag{11}$$

The sediment conservation equation is obtained by substituting (11) into (1),

$$\frac{\partial C}{\partial t} = w_0 \frac{\partial C}{\partial z} + \frac{\partial}{\partial z}\varepsilon_s \frac{\partial C}{\partial z} - \frac{\partial}{\partial z} P\left(t - \frac{z}{w_c}\right) F(z) \tag{12}$$

Time averaging and integrating the above equation with respect to z results in

$$w_0\bar{C} + \varepsilon_s \frac{d\bar{C}}{dz} - \bar{P}F(z) = 0 \tag{13}$$

where the following boundary conditions have been applied:

$$\left.\begin{aligned}\bar{C} &= 0 \\ d\bar{C}/dz &= 0 \\ F(z) &= 0\end{aligned}\right\} \quad z \to \infty \tag{14}$$

Assuming that $\varepsilon_s(d\bar{C}/dz)$ vanishes and $F(z)$ approaches 1 at the reference level, we get the following expression:

$$\bar{P} = w_0\bar{C}_r \tag{15}$$

The assumption that $\varepsilon_s(d\bar{C}/dz)$ vanishes at the reference level is a reasonable approximation, though not exact. As the bed is asymptotically approached, ε_s approaches zero and $d\bar{C}/dz$ approaches a constant value, so their product approaches zero. By substituting (15) into (13) and rearranging it, the following nonhomogeneous ordinary differential equation is obtained:

$$\frac{d\bar{C}}{dz} + \frac{w_0}{\varepsilon_s}\bar{C} = \frac{\bar{C}_r w_0}{\varepsilon_s} F(z) \tag{16}$$

Substitution of (4) for the eddy diffusivity in (16) results in the following three expressions:

$$\frac{d\bar{C}}{dz} + \frac{w_0}{\kappa u_{*cw} z}\bar{C} = \frac{\bar{C}_r w_0}{\kappa u_{*cw} z} F(z) \qquad z \le \alpha\delta \tag{17a}$$

$$\frac{d\bar{C}}{dz} + \frac{w_0}{\kappa u_{*cw}\alpha\delta}\bar{C} = \frac{\bar{C}_r w_0}{\kappa u_{*cw}\alpha\delta}F(z) \quad \alpha\delta \le z \le \alpha\delta/\varepsilon \quad (17b)$$

$$\frac{d\bar{C}}{dz} + \frac{w_0}{\kappa u_{*c} z}\bar{C} = \frac{\bar{C}_r w_0}{\kappa u_{*c} z}F(z) \quad \alpha\delta/\varepsilon \le z \quad (17c)$$

The solutions to (17a)–(17c) are

$$\frac{\bar{C}(z)}{\bar{C}_r} = z^{-a}\left[a\int_{z_r}^{z} z^{a-1}F(z)\,dz + \text{const1}\right] \quad (18a)$$

$$z \le \alpha\delta$$

$$\frac{\bar{C}(z)}{\bar{C}_r} = e^{-az/\alpha\delta}\left[\frac{a}{\alpha\delta}\int_{\alpha\delta}^{z} e^{az/\alpha\delta}F(z)\,dz + \text{const2}\right] \quad (18b)$$

$$\alpha\delta \le z \le \alpha\delta/\varepsilon$$

$$\frac{\bar{C}(z)}{\bar{C}_r} = z^{-a/\varepsilon}\left[\frac{a}{\varepsilon}\int_{\alpha\delta/\varepsilon}^{z} z^{a/\varepsilon\ -1}F(z)\,dz + \text{const3}\right] \quad (18c)$$

$$\alpha\delta/\varepsilon \le z$$

where const1, const2, and const3 are integration constants, and as before, a is $w_0/\kappa u_{*cw}$. The constants are found by applying the boundary condition at the reference level, $z = z_r$, and the matching conditions at $z = \alpha\delta$ and $z = \alpha\delta/\varepsilon$, yielding

$$\text{const1} = z_r^a \quad (19a)$$

$$\text{const2} = \left(\frac{\alpha\delta}{e}\right)^{-a}\left[a\int_{z_r}^{\alpha\delta} z^{a-1}F(z)\,dz + z_r^a\right] \quad (19b)$$

$$\text{const3} = \left(\frac{e\varepsilon}{\alpha\delta}\right)^{-a/\varepsilon}\left\{\left[\frac{a}{\alpha\delta}\int_{\alpha\delta}^{\alpha\delta/\varepsilon} e^{az/\alpha\delta}F(z)\,dz\right] + \left(\frac{\alpha\delta}{e}\right)^{-a}\left[a\int_{z_r}^{\alpha\delta} z^{a-1}F(z)\,dz + z_r^a\right]\right\} \quad (19c)$$

The combined convection-diffusion model consists of (18) and (19). Equation (10) will be used for $F(z)$ in the present study. If we set $F(z)$ to zero, (18) becomes identical to (5) of the pure diffusion model. If one wished to include the minor contribution of diffusion at the reference level, then (15) would be replaced by

$$\bar{P} = w_0\bar{C}_r + \left[\varepsilon_s\frac{d\bar{C}}{dz}\right]_r \quad (15')$$

The net result is a small increase in the reference concentration, so that in the final solutions, $\bar{C}_r$ is replaced by $\bar{C}_r + [1/C(d\bar{C}/dz)]_r$ on the left-hand side of (18). The form of the vertical distribution is unchanged.

Comparison of Model Results With Field Observations

A field experiment was conducted in the nearshore zone of Vilano Beach, St. Johns County, Florida, from March 22 to April 9, 1992 [*Lee*, 1994]. The objective of the experiment was to obtain comprehensive sets of data on the small-scale mechanisms of sediment suspension under a variety of combined wave and current conditions. Vilano Beach is on a barrier island bounded by the Atlantic Ocean to the east, Intracoastal Waterway to the west, and St. Augustine Inlet to the south. The primary sand dune is well developed and has a height of approximately 3 m. The face of the dune is well covered with vegetation. There is no shore protection structure or littoral barrier at or near the site. The orientation of the shoreline is approximately 21° counterclockwise from the north (see Figure 2).

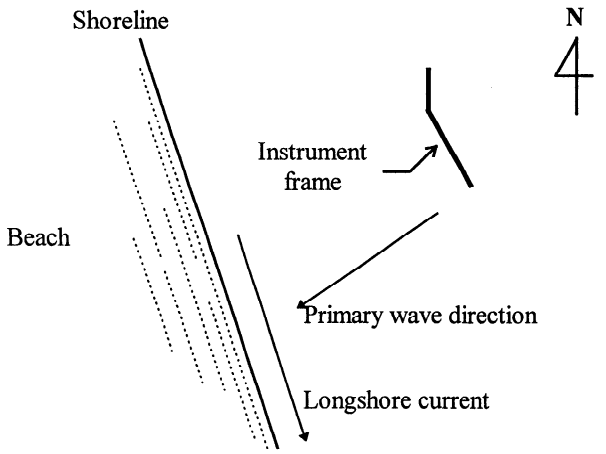

Figure 2. Orientation of shoreline, longshore current, wave, and instrument frame. The orientation of the shoreline and the crossbar of the instrument frame are approximately 21° and 28° counterclockwise from north, respectively.

The beach profile shown in Figure 3 was surveyed from the foot of the sand dune to the location of the instrument on April 10, 1992. The average slope over the distance from the offshore end of the berm and the deepest point before the offshore bar is 5.9%. The offshore bar is usually located just outside the surf zone.

The bed material in the immediate vicinity of the instruments was sampled by divers. The result of the sieve analysis is summarized in Table 1. Almost all of the sample in sieve numbers 10 and 20 is shell fraction. This portion was not considered for the analysis of fall velocity distribution because it is assumed that under the wave conditions encountered during the experiment, the shell remained on the bed. The shell fragment was not used for the calibration of acoustic system due to the same considerations. The median diameter d_{50} of the bed material finer than sieve number 20 is 0.144 mm. Fall velocity of the bed material was measured in a settling tube. The proportion by weight for each fall velocity is listed in Table 2.

Configuration of the Measurement System

The instruments were deployed at the offshore slope of the offshore bar in a water depth of approximately 3.3 m. Instruments were supplied with power and controlled through 300-m-long cables from the shore station. Figure 4 shows the overall configuration of the field measurement system. One pressure sensor, one electromagnetic current meter (EMCM), and two optical backscatter sensors are directly connected to the Tattletale model VI data logger. These instruments are synchronized with the acoustic concentration profiler (ACP). The software in the data logger controls the ACP through the

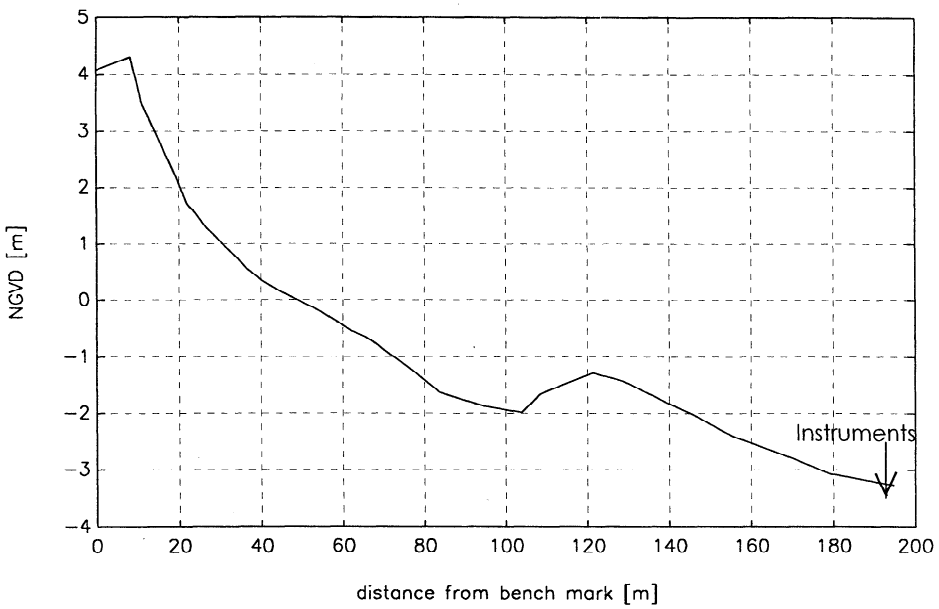

Figure 3. Profile at Vilano Beach on April 10, 1992.

interface board and the other instruments directly. The analog signal from the ACP is digitized by the interface board. The signals from the other instruments are digitized at the data logger. All the instruments and the data logger are powered by rechargeable batteries. The batteries are charged continuously through the cable from the shore station. The voltage of the batteries is monitored at the shore station.

Acoustic backscatter allows continuous measurement of the concentration profile of suspended sediment with high resolution in time and space without disturbing the measurement region [*Hanes et al.*, 1988]. It is also possible to measure the change of the bed location synchronously and continuously. This capability is important because an error in the bed location can introduce a significant error in measurement of sediment concentration near the seabed due to the large concentration gradient. The ACP used in this experiment was a Simrad Mesotech model 810, with specifications as listed in Table 3. The temporal and spatial resolution of the ACP data is 1 Hz and 3 mm, respectively. The sampling rate of the other instruments is 2 Hz.

Table 1. Sieve Analysis of Bed Material

Sieve Number	Mesh Size, mm	Percent Retained
10	2.000	1.1
20	0.840	1.0
30	0.590	0.3
40	0.420	0.5
50	0.300	0.8
60	0.250	0.7
70	0.210	2.0
80	0.177	9.6
100	0.149	27.6
120	0.125	35.6
140	0.105	11.9
160	0.097	4.9
Pan	NA	4.1
Total	...	100

NA is not applicable.

The ACP was calibrated in the laboratory using sand samples taken from the field. Over the range of approximately 50 to 1000 mg/L, which were the conditions found most frequently in the field, the laboratory calibration was accurate to approximately 20%. For concentrations between 1 and 20 g/L the calibration became less accurate and errors increased with distance from the transducer (the concentration field in the calibration tank was uniform in space). The decrease in accuracy for high concentrations and increasing range is related to a number of factors including the scattering of sound by multiple targets, decreasing signal to noise due to the scattering and absorption of sound, and transducer nonlinearities at low signal strength. Further details on the principles of operation of the ACP, its calibration, and its accuracy are given by *Lee and Hanes* [1995] and *Thorne et al.* [1993].

Underwater installation of instruments is illustrated in Figure 4. The orientation of the crossbar was 28° counterclockwise from the north as shown in Figure 2. The elevations of the instruments above the bed on April 1, 1992, are listed in Table 4. The elevations are not constant because the bed location changes due to erosion or deposition. However, the relative distances between the instruments are constant. The instantaneous bed location is measured by the ACP. The instantaneous elevation of the other instruments is easily determined. The

Table 2. Fall Velocity

Fall Velocity, cm/s	Proportion by Weight, %
0.95	9.2
1.2	12.2
1.6	36.5
2.2	28.2
2.7	9.8
3.0	2.1
3.1	0.7
3.5	1.4
Total	100

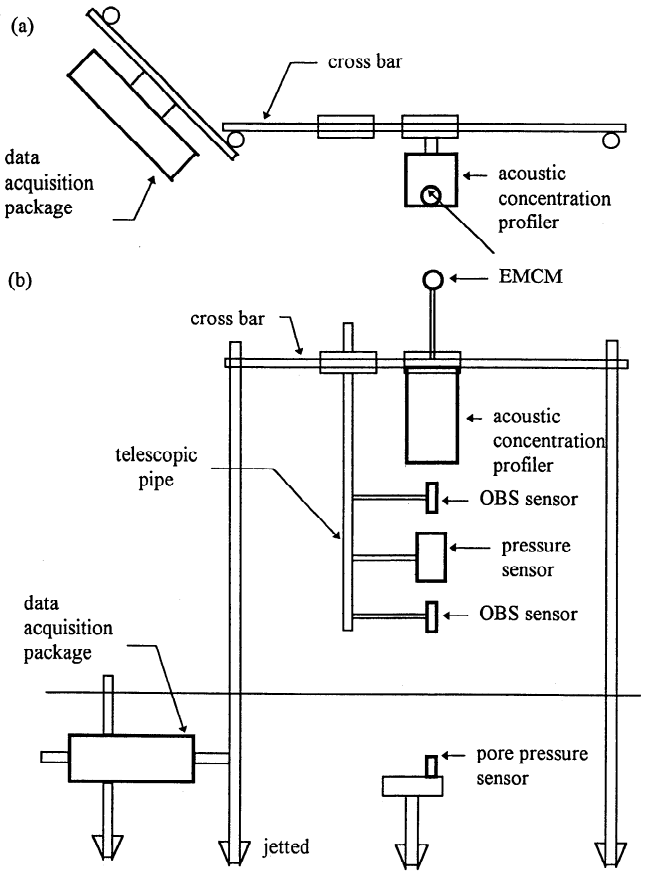

Figure 4. Underwater deployment of the instruments from (a) plan view and (b) front view, seen toward the ocean from the shore.

underwater data acquisition package was buried below the bed surface.

Field Data Analysis

The vertical distribution models referred to earlier have been developed for monochromatic wave conditions. Because the basic equations are linear, the models could be applied to broadband wave forcing in a linear manner. However, such an extension is not warranted for the present analysis because our goals are to attempt to describe which of the two basic mixing processes are most applicable and under what conditions. To this end, we apply the models to the field data by approximating the wave forcing by an equivalent monochromatic wave, closely following *Madsen and Wikramanayake* [1991].

Table 3. Specifications of the Simrad Model 810 Acoustic Concentration Profiler

Parameter	Specification
Acoustic pulse	excitation frequency, 5 MHz; duration, 10 μs; repetition rate, 100 Hz
Time-varying gain, dB	20 $\log_{10}$ $(r/7)$ + 20, where r is range in millimeters
Output signal	455 kHz, amplitude modified
Diameter of transducer	0.32 cm
Near-field limit	10.7 cm (theoretical value)

Table 4. Elevation of Instruments Above Bed on April 1, 1992

Instrument	Elevation Above Bed, m
EMCM	1.45
ACP	1.02
OBS sensor	0.81
Pressure sensor	0.74
OBS sensor	0.30

Abbreviations are EMCM, electromagnetic current meter; ACP, acoustic concentration profiler; and OBS, optical backscatter sensor.

The EMCM data are decomposed into current velocity $\bar{u}$, $\bar{v}$ and wave velocity $\tilde{u}$, $\tilde{v}$,

$$u(z_c, t) = \bar{u}(z_c) + \tilde{u}(z_c, t);$$
$$v(z_c, t) = \bar{v}(z_c) + \tilde{v}(z_c, t) \tag{20}$$

where u and v denote the cross-shore and longshore components of the fluid velocity, respectively. The elevation of the EMCM is denoted by z_c. The overbar and the tilde indicate the time mean and oscillating components of the fluid velocities, respectively. The positive directions of the longshore and the cross-shore components of EMCM data are 28° and 118° counterclockwise from the north, respectively.

The wave velocity near the bed can be calculated with the wave velocity at $z = z_c$ by using linear wave theory. The time series of the wave velocity at the elevation of the EMCM is transformed by fast Fourier transfer (FFT) as follows:

$$\tilde{U}(z_c, \omega) = \text{FFT}\{\tilde{u}(z_c, t)\};$$
$$\tilde{V}(z_c, \omega) = \text{FFT}\{\tilde{v}(z_c, t)\} \tag{21}$$

where $\tilde{U}$ and $\tilde{V}$ are complex quantities. The wave number of each frequency component is calculated with the dispersion relationship. The quantity near the bed in the frequency domain is found with the following equation:

$$\tilde{U}(0, \omega) = \frac{\tilde{U}(z_c, \omega)}{\cosh kz_c}; \qquad \tilde{V}(0, \omega) = \frac{\tilde{V}(z_c, \omega)}{\cosh kz_c} \tag{22}$$

The time series of the wave velocity near the bed is found by applying inverse FFT to $\tilde{U}(0, \omega)$ and $\tilde{V}(0, \omega)$,

$$\tilde{u}(0, t) = \text{inverse FFT}\{\tilde{U}(0, \omega)\};$$
$$\tilde{v}(0, t) = \text{inverse FFT}\{\tilde{V}(0, \omega)\} \tag{23}$$

The primary wave direction is determined by finding the direction in which the variance of the wave velocity near the bed is a maximum. Figure 5 shows the definition of the directions of the primary wave direction and the calibrated EMCM data. The cross-shore and longshore components of the EMCM data are denoted by $\tilde{u}$ and $\tilde{v}$, respectively. Those of primary wave directions are labeled by $\tilde{u}_p$ and $\tilde{v}_p$.

If we imagine that the coordinate system of the EMCM was rotated counterclockwise by θ, then the horizontal velocity components on the new coordinate system, $\bar{u}'$ and $\bar{v}'$, can be expressed as the product of the rotation matrix and the components on the original coordinate system, $\bar{u}$ and $\bar{v}$,

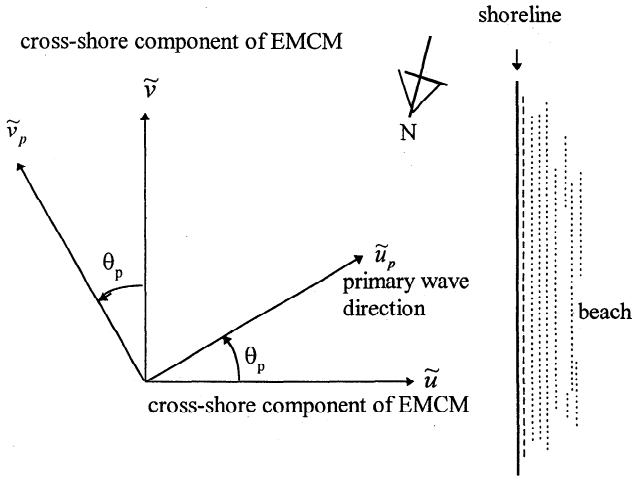

Figure 5. Definition sketch of the primary wave direction.

$$\begin{bmatrix} \tilde{u}' \\ \tilde{v}' \end{bmatrix} = \begin{bmatrix} \cos\theta & \sin\theta \\ -\sin\theta & \cos\theta \end{bmatrix} \begin{bmatrix} \tilde{u} \\ \tilde{v} \end{bmatrix} \tag{24}$$

The rotation angle of the coordinate system of the primary wave θ_p must satisfy the following conditions according to its definition:

$$\left.\frac{\partial E[(\tilde{u}')^2]}{\partial\theta}\right|_{\theta=\theta_p} = 0, \qquad \left.\frac{\partial^2 E[(\tilde{u}')^2]}{\partial\theta^2}\right|_{\theta=\theta_p} < 0 \tag{25}$$

By applying (24) and (25) to the time series of (23), the angle between the cross-shore component of the EMCM and the primary wave direction near the bed θ_p can be found in the following expressions:

$$\theta_p = \begin{cases} \dfrac{1}{2}\arctan\left(\dfrac{2\sum_{n=1}^{N}\tilde{u}_n\tilde{v}_n}{\sum_{n=1}^{N}\tilde{v}_n^2 - \tilde{u}_n^2}\right), & F(\theta_p) < 0 \\ \dfrac{1}{2}\arctan\left(\dfrac{2\sum_{n=1}^{N}\tilde{u}_n\tilde{v}_n}{\sum_{n-1}^{N}\tilde{v}_n^2 - \tilde{u}_n^2}\right) + \dfrac{\pi}{2}, & F(\theta_p) > 0 \end{cases} \tag{26}$$

where $\tilde{u}_n$ and $\tilde{v}_n$ are the cross-shore and longshore components of the wave velocity near the bed at time $t = t_n$, respectively, and

$$F(\theta_p) = \sum_{n=1}^{N} (\tilde{v}_n^2 - \tilde{u}_n^2)\cos 2\theta_p - 2\tilde{u}_n\tilde{v}_n \sin 2\theta_p.$$

The velocity components $\tilde{u}_p$ and $\tilde{v}_p$ of the primary directions are found by substituting (26) into (24).

The peak wave frequency is estimated as the mean zero-crossing wave frequency, defined as the following:

$$\omega_0 = \sqrt{\frac{\int S_{uu}(\omega)\omega^2\, d\omega}{\int S_{uu}(\omega)\, d\omega}} \tag{27}$$

where $S_{uu}(\omega)$ is the power spectrum of the wave velocity near the bed in the primary wave direction. The amplitude of the wave velocity is calculated in the following fashion:

$$\hat{u}_p = \sqrt{2}\sqrt{\frac{1}{N}\sum_{n=1}^{N}\tilde{u}_{p,n}^2} \tag{28}$$

where $\tilde{u}_{p,n}$ is the wave velocity near the bed at $t = t_n$ in the primary wave direction. It was assumed that the wave velocity and its amplitude follow normal and Rayleigh distributions, respectively. The angle ϕ_{cw} is measured counterclockwise from the primary wave direction to the current.

It is necessary to estimate the friction velocities and ripple geometry in order to use the two models reviewed and the combined model developed in this study. They were not measured in the field but calculated with the turbulent wave-current bottom boundary layer model of *Madsen and Wikramanayake* [1991].

The model uses the eddy viscosity profile which is exactly the same as the eddy diffusivity profile in (4). The current profile is described by the following equation:

$$\bar{u}(\zeta) = \begin{cases} \varepsilon\dfrac{u_{*c}}{\kappa}\ln\dfrac{\zeta}{\zeta_0}, & \zeta_0 \le \zeta < \alpha \\ \varepsilon\dfrac{u_{*c}}{\kappa}\left[\dfrac{\zeta}{\alpha} - 1 + \ln\dfrac{\alpha}{\zeta_0}\right], & \alpha \le \zeta \le \alpha/\varepsilon \\ \dfrac{u_{*c}}{\kappa}\left[\ln\dfrac{\varepsilon\zeta}{\alpha} + 1 + \varepsilon\left(\ln\dfrac{\alpha}{\zeta_0} - 1\right)\right], & \alpha/\varepsilon \le \zeta \end{cases} \tag{29}$$

where ε is the ratio of u_{*c} to u_{*cw} and $\zeta_0 = z_0/\delta = k_b/30\delta$.

The wave velocity profile is described by the following equations:

$$\begin{aligned} u_d &= A_1[\mathrm{Ker}\ 2\sqrt{\zeta} + i\ \mathrm{Kei}\ 2\sqrt{\zeta}] \\ &\quad + A_2[\mathrm{Ber}\ 2\sqrt{\zeta} + i\ \mathrm{Bei}\ 2\sqrt{\zeta}], \qquad \zeta_0 \le \zeta < \alpha \\ u_d &= A_3\exp(\sqrt{i/\alpha\zeta}) + A_4\exp(-\sqrt{i/\alpha\zeta}), \qquad \alpha \le \zeta < \alpha/\varepsilon \end{aligned} \tag{30}$$

$$\begin{aligned} u_d &= A_5[\mathrm{Ker}\ 2\sqrt{\zeta/\varepsilon} + i\ \mathrm{Kei}\ 2\sqrt{\zeta/\varepsilon}] \\ &\quad + A_6[\mathrm{Ber}\ 2\sqrt{\zeta/\varepsilon} + i\ \mathrm{Bei}\ 2\sqrt{\zeta/\varepsilon}], \qquad \alpha/\varepsilon \le \zeta \end{aligned}$$

by introducing the following complex velocity deficit function,

$$\mathrm{Re}\{u_d\exp(i\omega t)\} = \frac{\tilde{u}_b - \tilde{u}_p}{|\tilde{u}_p|} \tag{31}$$

where $\tilde{u}_b$ and $\tilde{u}_p$ are the wave velocity in the boundary layer and the free stream wave velocity near the bed, respectively, in the primary wave direction. The coefficients A_1 through A_6 are complex coefficients to be determined with the two boundary conditions

$$u_d = -1 \qquad z = z_0; \qquad u_d \to 0 \qquad z \to \infty \tag{32}$$

Table 5. Parameters of the Data Files for Comparison

Data Burst	Frequency, rad/s	$\hat{u}_p$, cm/s	$\bar{u}$, cm/s	ϕ_{cw}, deg	EMCM Height, cm	Water Depth, cm	Burst Length, s
1	1.64	29.5	12.6	56.5	140.7	363.6	223
2	1.34	28.4	19.9	63.2	141.1	275.9	291
3	1.40	26.3	20.2	64.0	141.1	272.4	351
4	1.40	28.2	18.3	61.4	141.0	267.6	268
5	1.42	57.2	43.2	59.7	141.6	393.9	210
6	1.32	61.2	52.4	48.3	141.5	381.5	123
7	1.32	69.6	61.7	58.9	141.7	371.5	252
8	1.40	66.6	63.6	65.7	141.7	361.3	134

Variables are $\hat{u}_p$, amplitude of the wave velocity; $\bar{u}$, time mean of the cross-shore component of fluid velocity; ϕ_{cw}, the angle measured counterclockwise from the primary wave direction to the current.

and the four matching conditions of velocity and its gradient at $\zeta = \alpha$ and $\zeta = \alpha/\varepsilon$. The six coefficients are determined with the following six equations:

$$A_1(\mathrm{Ker}\ 2\sqrt{\zeta_0} + i\ \mathrm{Kei}\ 2\sqrt{\zeta_0}) + A_2(\mathrm{Ber}\ 2\sqrt{\zeta_0} + i\ \mathrm{Bei}\ 2\sqrt{\zeta_0}) = -1 \tag{33a}$$

$$A_6 = 0 \tag{33b}$$

$$A_1(\mathrm{Ker}\ 2\sqrt{\alpha} + i\ \mathrm{Kei}\ 2\sqrt{\alpha}) + A_2(\mathrm{Ber}\ 2\sqrt{\alpha} + i\ \mathrm{Bei}\ 2\sqrt{\alpha}) = A_3 e^{\sqrt{i\alpha}} + A_4 e^{-\sqrt{i\alpha}} \tag{33c}$$

$$A_1(\mathrm{Ker}'\ 2\sqrt{\alpha} + i\ \mathrm{Kei}'\ 2\sqrt{\alpha}) + A_2(\mathrm{Ber}'\ 2\sqrt{\alpha} + i\ \mathrm{Bei}'\ 2\sqrt{\alpha}) = A_3\sqrt{ie}^{\sqrt{i\alpha}} - A_4\sqrt{ie}^{-\sqrt{i\alpha}} \tag{33d}$$

$$A_3 e^{\sqrt{i\alpha/\varepsilon}} + A_4 e^{-\sqrt{i\alpha/\varepsilon}} = A_5(\mathrm{Ker}\ 2\sqrt{\alpha/\varepsilon} + i\ \mathrm{Kei}\ 2\sqrt{\alpha/\varepsilon}) \tag{33e}$$

$$A_3\sqrt{ie}^{\sqrt{i\alpha/\varepsilon}} - A_4\sqrt{ie}^{-\sqrt{i\alpha/\varepsilon}} = A_5(\mathrm{Ker}'\ 2\sqrt{\alpha/\varepsilon} + i\ \mathrm{Kei}'\ 2\sqrt{\alpha/\varepsilon}) \tag{33f}$$

The six coefficients above are expressed in terms of α, ε, and ζ_0. The parameter ε is the ratio of the current friction velocity to the wave-current friction velocity. The nondimensional height ζ_0 is proportional to the ratio of the equivalent Nikuradse roughness to the boundary layer thickness scale k_b/δ, in which k_b is a function of ripple geometry and δ is proportional to the wave-current friction velocity. Therefore solving the combined wave-current problem is equivalent to finding the friction velocities and ripple geometry.

On the basis of *Wikramanayake*'s [1993] summary and analyses of the field data by *Boyd et al.* [1988], *Nielsen* [1984], *Miller and Komar* [1980], *Dingler* [1974], and *Inman* [1957], the following formulas are used to predict the ripple height and ripple steepness:

$$\eta = \begin{cases} 0.018A_bZ^{-0.5}, & 0.0016 \le Z < 0.012 \\ 0.0007A_bZ^{-1.23}, & 0.012 \le Z < 0.18 \\ 0, & 0.18 \le Z \end{cases} \tag{34}$$

$$\frac{\eta}{\lambda} = \begin{cases} 0.15Z^{-0.01}, & 0.016 \le Z < 0.012 \\ 0.014Z^{-0.55}, & 0.012 \le Z < 0.18 \\ 0, & 0.18 \le Z \end{cases} \tag{35}$$

where η and λ are ripple height and length, respectively, and A_b is defined by $\hat{u}_p/\omega_0$. The nondimensional quantity Z is defined as

$$Z = \frac{\theta'_w}{S_*}; \qquad S_* = \frac{1}{4\nu}\sqrt{(s-1)gd_{50}^3} \tag{36}$$

where ν is the kinematic viscosity of the fluid, θ'_w is the Shields parameter based on wave skin friction velocity, and s is the specific gravity of the sediment. The equivalent Nikuradse roughness is estimated as 4η in the rippled bed regime, d_{50} in the quiescent flat bed regime, and $10\ d_{50}$ in the sheet flow regime.

Field Observations and Model Comparisons

Eight data bursts were selected for data comparisons. These data sets, summarized in Table 5, were chosen to represent a variety of wave and current conditions. They were also selected for periods in which the bottom location did not change during the burst, thus ensuring that there were no local horizontal gradients in the sediment flux. The primary direction of incident waves was from the northeast during the experiment. The rms wave height ranges approximately from 0.4 m for calm conditions to 1.2 m for rough conditions. The direction of longshore current was mainly from north to south during the field measurements, with a magnitude ranging from 0.1 to 1.4 m/s. The tide is semidiurnal, with a range of approximately 1.4 m. There were no rip currents observed at the site during the measurement. The water temperature was approximately 16 to 19°C. The visibility near the instruments was generally less than 1 m.

The system of (29), (30), and (33)–(36) was solved with the iteration method of *Wikramanayake* [1993], with results shown in Table 6. The shear stresses for all runs exceed the threshold of motion, and for the latter four runs, sheet flow conditions were most likely in place. The ripples, when they were present, are predicted to have been only 2 to 3 mm in height. These small ripples are consistent with diver observations during periods with similar wave conditions. Although the ripples are small, they are significant when compared to either the sand grain diameter or the length scale of a viscous boundary layer over a flat wall. Therefore even these small ripples can be expected to influence the generation of vorticity and the mixing processes in their immediate vicinity.

The pure diffusion model and the combined model for the mean concentration profile were applied to eight bursts of Vilano Beach data using the median grain size and fall velocity. The same models were also applied with fall velocity classes in order to examine the effect of suspending material preferen-

Table 6. Estimated Ripple Geometry, Equivalent Roughness, and Friction Velocities

Data Burst	η, cm	η/λ	k_b, cm	u_{*c}, cm/s	u_{*w}, cm/s	u_{*cw}, cm/s	z_1, cm
1	0.171	0.046	0.68	0.84	3.94	3.99	1.35
2	0.229	0.049	0.92	1.17	3.91	4.00	1.44
3	0.231	0.052	0.92	1.17	3.73	3.82	1.41
4	0.217	0.049	0.87	1.08	3.88	3.96	1.38
5	0.000	0.000	0.14	2.30	5.06	5.35	1.32
6	0.000	0.000	0.14	2.73	5.39	5.87	1.23
7	0.000	0.000	0.14	3.15	5.97	6.45	1.44
8	0.000	0.000	0.14	3.16	5.78	6.21	1.41

Variables are η, ripple height; λ, ripple length; k_b, equivalent Nikuradse roughness; u_{*c}, current friction velocity; u_{*w}, wave friction velocity; u_{*cw}, combined wave-current friction velocity; and z_1, concentration measurement point closest to the bottom.

tially according to its size. Each of the fall velocities in Table 2 was used to calculate the corresponding concentration profiles. The calculated profile was weight-averaged by the proportion in Table 2 to yield a concentration profile with multiple fall velocity classes. Each time-averaged concentration profile observed or calculated was normalized with the concentration measurement point closest to the bottom (z_1 in Table 6) to compare the shape of the profiles only.

When the pure convection model was applied to the field data, the following formula by *Nielsen* [1992] was used to calculate the equivalent Nikuradse roughness:

$$k_b = 8\eta^2/\lambda + 5\theta_{2.5}d_{50} \tag{37}$$

where

$$\theta_{2.5} = \frac{1}{2}\frac{f_{2.5}\hat{u}_p^2}{(s-1)gd_{50}}$$

$$f_{2.5} = \exp\left[5.213(2.5d_{50}/A_b)^{0.194} - 5.977\right]$$

which is the formula developed by *Swart* [1974].

In Figures 6a–6d, four sets of field observations under low wave energy conditions are compared with the model results. The solid lines (without symbols) represent the observations. The solid lines with circles are the results by the pure convection model. The solid lines with pluses indicate the results by the pure diffusion model using the median fall velocity. The dashed lines are the results by the pure diffusion model using multiple fall velocity classes which are shown in Table 2. The results by the combined convection-diffusion model using the median fall velocity and multiple fall velocity classes are represented by the solid and dashed lines with asterisks, respectively.

For these four bursts the pure convection model is the most accurate in predicting the vertical distribution of suspended sediment concentration. Its predictions are excellent up to 10 cm above the bed. The predictions by the diffusion model using a single fall velocity is the least accurate. Using multiple fall velocity groups improved the diffusion model somewhat, but the predictions are far less accurate than the predictions by the pure convection model. The combined model predicts the concentration profiles much better than the pure diffusion model. The results of the combined model are improved a little by the use of multiple fall velocity classes. It is interesting that the use of multiple size fractions tends to decrease the predicted concentration gradients relative to the results using only the median size. This is because the smaller particles are more easily mixed and remain in suspension longer than the coarser particles, particularly under low wave conditions. This trend is consistent with observed data, which indicate small concentration gradients higher than 10 cm above the bed. However, the observed gradients in this region are quantitatively smaller than the predictions of any of the models. The explanation for this discrepancy is unknown. The most likely explanation is related to the selective entrainment of fine sediment from the bed, particularly under low wave conditions. There is some consolation in the fact that the concentration is relatively small above 10 cm.

Figures 7a–7d show the predictions by the models and the field observations under high wave energy conditions. The line patterns and marks are the same as in Figure 6. The pure diffusion model using multiple fall velocity groups predicts the distribution excellently up to 30 cm above the bed; however, it shows a tendency toward slight overprediction at 10 to 15 cm above the bed. The pure convection model considerably underpredicts the distribution at almost all the elevations, except below 5 cm. The predictions by the pure diffusion model using the median fall velocity run between the above two model results, except for Figure 7a, in which its prediction is almost identical to that by the convection model. The results of the combined model are very similar to those of the pure diffusion model. However, the results of the combined model using the median fall velocity are always better than those of the diffusion model using the median fall velocity or those of the convection model. The use of multiple fall velocity classes greatly improves the results of the combined model.

Under high wave energy conditions it appears that the diffusion model predicts the vertical distribution of the suspended sediment better than the convection model and that the use of multiple fall velocity groups helps predict the distribution more accurately. Conversely, the convection model works better than the diffusion model under low wave energy conditions. The combined model under low energy conditions works better than the diffusion model, but under high energy conditions the results are almost the same.

Discussion

While the application of monochromatic models to field observations is somewhat crude, the results are quite useful in evaluating the dominant mixing processes under various conditions. If our goal was to predict the suspended sediment concentration as accurately as possible, then it would be advantageous to more carefully treat the multifrequency aspects of the fluid forcing as done, for example, by *Wikramanayake*

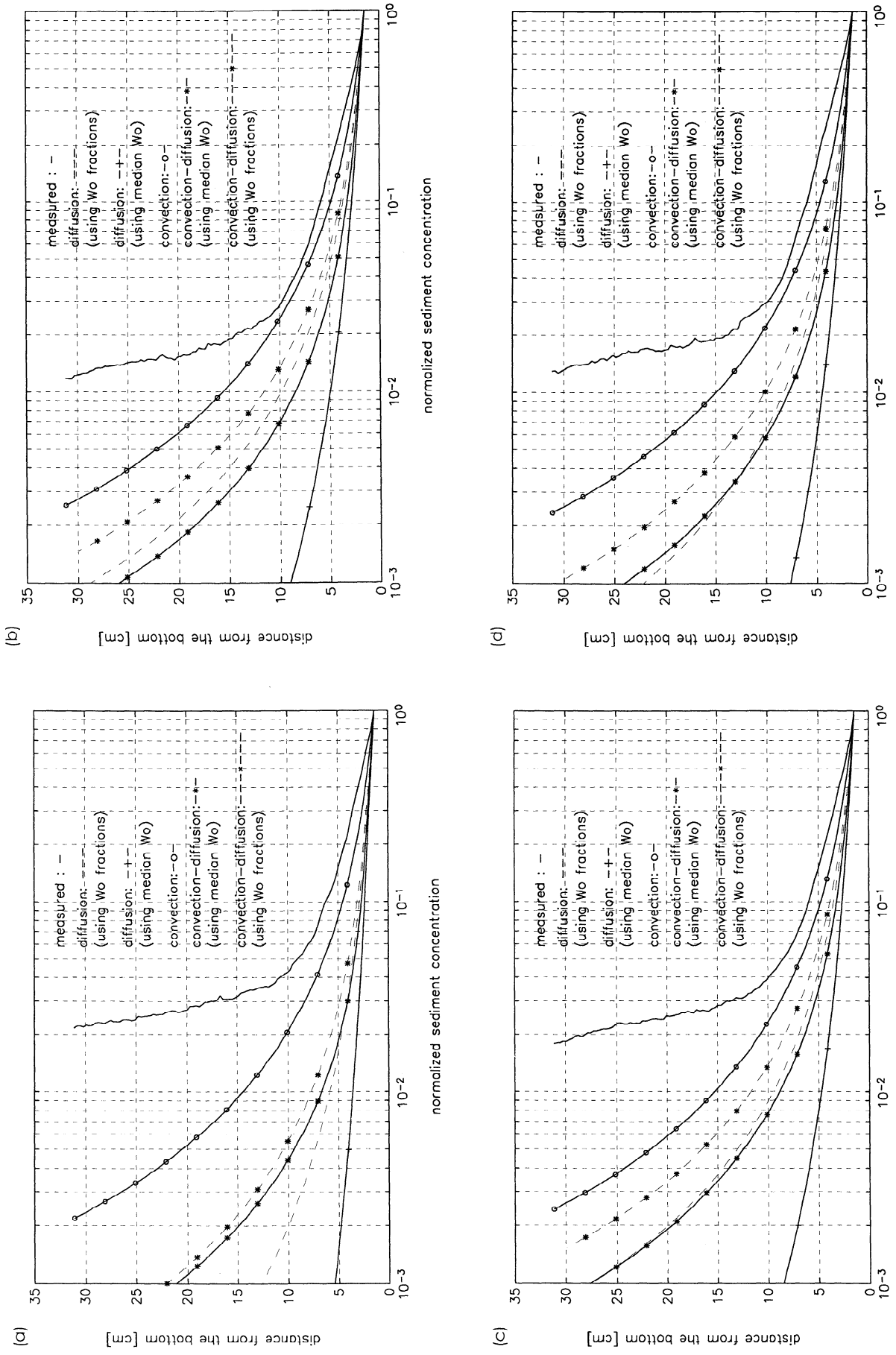

Figure 6. Distribution of suspended sediment under low wave energy conditions for (a) burst 1, (b) burst 2, (c) burst 3, and (d) burst 4.

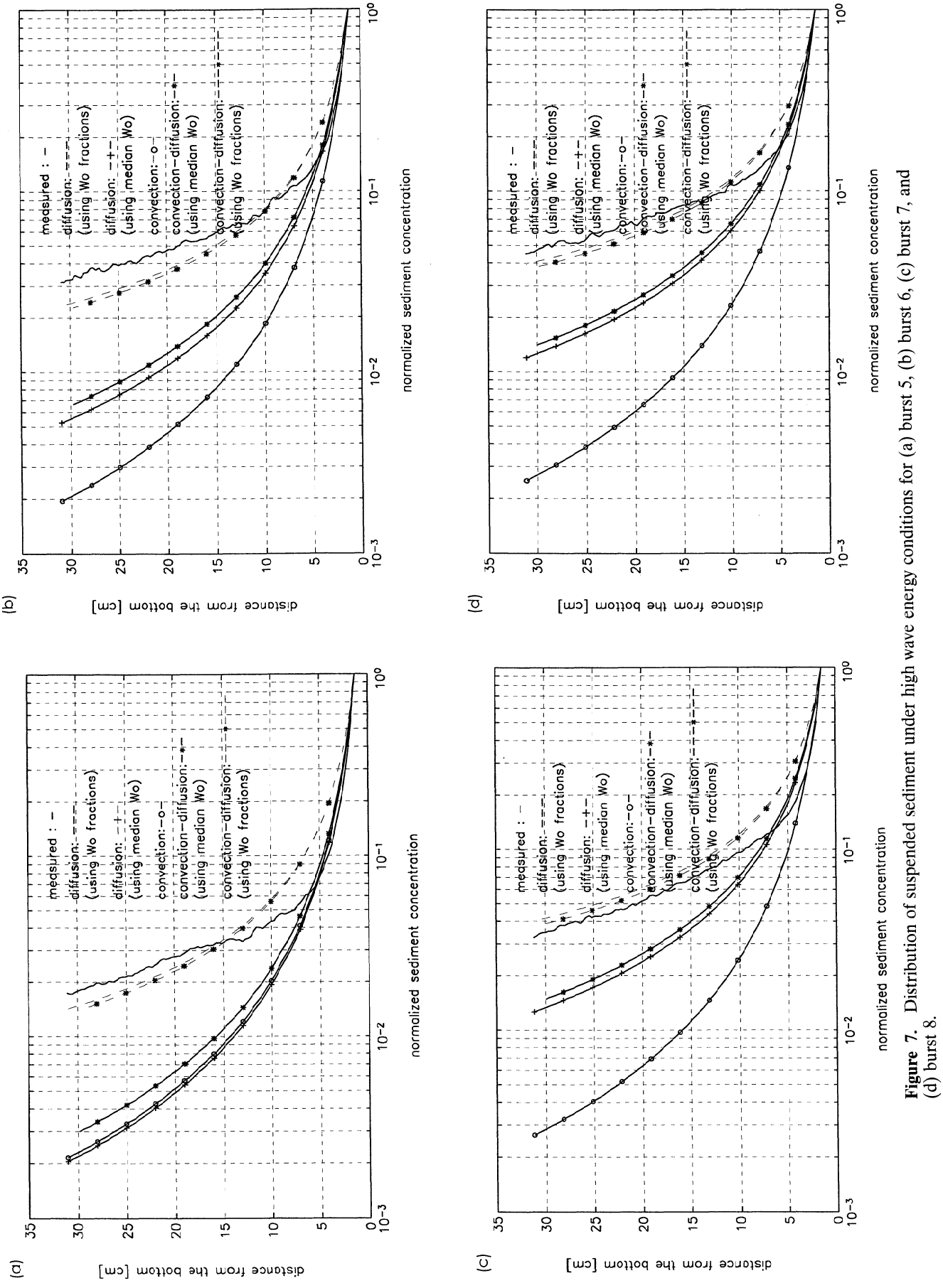

Figure 7. Distribution of suspended sediment under high wave energy conditions for (a) burst 5, (b) burst 6, (c) burst 7, and (d) burst 8.

[1993]. However, our analysis is oriented toward evaluating the significance of the various mixing processes and the conditions under which each process dominates over the other. In applying the models, there are a number of adjustable parameters. We chose not to adjust any of these parameters but, rather, to use all of the values suggested in the original publications of the models, except that the profiles are normalized by the reference concentration. Again, this approach seems reasonable, given the goals of this effort.

The bedform conditions play a crucial role in interpreting these observations. The bed forms model predicts that the beds of Figures 6a–6d have ripples and those of Figures 7a–7d are flat (see Table 6). This suggests that the diffusion model works well over flat beds and the convection model does well over rippled beds. It is reasonable to conclude that convection is predominant over turbulent diffusion in transporting the suspended sediment upward above the rippled beds and that the opposite is true above the flat beds.

The lee vortex released from the ripple at the free stream reversal is one of the plausible mechanisms that supports the convection model. It has been long known that the convective mixing by lee vortices is very effective in transporting suspended sediment over rippled beds [e.g., *Hom-ma and Horikawa*, 1963]. It is probable that most of the sediment particles get trapped in the lee vortices and are lifted up to higher elevations over the rippled beds under low wave energy conditions.

Under high wave energy conditions the ripples wash away and the bed transport mode goes into sheet flow regime. Individual particles may be ejected out of the sheet flow due to intergranular collisions and transported upward by the turbulent diffusion. The fluid turbulence in the sheet flow is probably weaker than above because of the dense concentration of sediment particles. This difference in turbulence at the top of the sheet flow can help the particles be entrained into the water column easily. Therefore turbulent diffusion is probably the most dominant mechanism responsible for the sediment suspension under high (but nonbreaking) wave energy conditions. As (3) indicates, the diffusion is strongly dependent on the fall velocity of the sediment particles. Therefore the excellent agreement between the field observation and the results of the pure diffusion model using multiple fall velocity groups as shown in Figures 6a–6d also implies that the diffusion is most responsible for the suspension under high energy conditions.

In contrast to diffusion, the convection process described earlier is not very sensitive to the fall velocity of the sediment particles. The two processes have differences not only in the mixing scale, but also in the physics as discussed above. If the convection process is forced to be described by a diffusion model, then the eddy viscosity profile must vary with the particle fall velocity. The only way in which (3) is independent of the fall velocity is that the eddy diffusivity is linearly proportional to the fall velocity. *Nielsen* [1990] suggested a convective mixing length scale in order to extend the validity of (3) and to model the sediment suspension over sharp-crested ripples. His mixing length scale turned out to be inversely proportional to the fall velocity for low wave energy conditions. *Fredsoe and Deigaard* [1992] also showed in their theoretical work why the apparent eddy viscosity becomes dependent on the size of particles in suspension (or the fall velocity) when the convective mixing is modeled with pure gradient diffusion.

The predictions by the combined convection-diffusion model of the suspended sediment distribution under high wave energy conditions are almost the same as those by the pure diffusion model (see Figure 7) but are very different under low energy conditions (see Figure 6). The predictions by the combined model are not greatly improved by the use of multiple fall velocity classes under low energy conditions but are greatly improved under high energy conditions. This also can be interpreted that the convection processes are more responsible for the sediment suspension over rippled beds and that the diffusion processes are more responsible for the suspension over flat beds.

It seems safer to use the combined model rather than the pure diffusion model to predict the time-averaged vertical distribution of suspended sediment under wave-current flow. That is because the combined model under high energy conditions predicts almost the same as the pure diffusion model and much better under low energy conditions.

However, the combined model does not work better than the pure convection model for the examples under the low energy conditions. This might be due to either an inappropriate eddy diffusivity profile $\varepsilon_s(z)$, an inappropriate form of the entrainment probability distribution $F(z)$, or the assumption that convection dominates diffusion at the reference height. However, the eddy diffusivity profile represented by (4) seems reasonably good because the pure diffusion model using multiple fall velocity classes works very well over flat beds. The function $F(z)$ used in this paper was developed by *Nielsen* [1992] with laboratory data over rippled beds. It has not been widely tested as yet. More investigation on the entrainment probability distribution should be performed under various flow conditions to improve the combined model. Perhaps discrete vortex modeling could be used effectively to develop more accurate models for the convection process.

Conclusions

Observations of the time-mean vertical distribution of suspended sediment concentration in a nearshore zone have been compared with model predictions. A pure diffusion model [*Wikramanayake*, 1993] is in good agreement with the field observations under high wave energy conditions but not under low wave energy conditions. A pure convection model [*Nielsen*, 1992] is in good agreement with the observations under low wave energy conditions but not under high wave energy conditions. The applicability of the combined model has a wider scope than the pure diffusion model or the pure convection model. From an engineering viewpoint the combined model is much safer to use than the pure diffusion model because the former predicts the sediment distribution over a flat bed almost the same as the latter and over a rippled bed much better.

It is highly recommended for future field measurements that the ripple geometry be measured in addition to the sediment concentration. The in situ measurement of the vertical structure of the representative sediment size can be made by using several acoustic sensors of different frequencies together. That way, the inversion of the acoustic data into sediment concentration will be more accurate. More research on the entrainment probability function over rippled beds and flat beds under various flow conditions will improve the applicability and accuracy of the combined convection-diffusion model.

Acknowledgments. The authors gratefully acknowledge the support of the Coastal Sciences Program, U.S. Office of Naval Research. T. H. Lee also wishes to acknowledge the support and encouragement

of the Daewoo Corporation. We would also like to thank N. Wikramanayake and O. Madsen for their cooperation and assistance in applying their models.

References

Bagnold, R. A., The flow of cohesionless grains in fluids, *Philos. Trans. R. Soc. London A*, *249*, 235–297, 1956.

Boyd, R., D. L. Forbes, and D. E. Heffler, Time-sequence observations of wave-formed sand ripples on an ocean shore face, *Sedimentology*, *35*, 449–464, 1988.

Dingler, J. R., Wave formed ripples in nearshore sands, Ph.D. dissertation, Univ. of Calif., San Diego, 1974.

Fredsoe, J., and R. Deigaard, *Mechanics of Coastal Sediment Transport*, World Sci., River Edge, N. J., 1992.

Grant, W. D., and O. S. Madsen, Combined wave and current interaction with rough bottom, *J. Geophys. Res.*, *84*(C4), 1797–1808, 1979.

Hanes, D. M., C. E. Vincent, D. A. Huntley, and T. L. Clarke, Acoustic measurements of suspended sand concentration in the C2S2 experiment at Stanhope Lane, Prince Edward Island, *Mar. Geol.*, *81*, 185–196, 1988.

Hom-ma, M., and K. Horikawa, Suspended sediment due to wave action, paper presented at Eighth Conference on Coastal Engineering, Counc. on Wave Res., Univ. of Calif., Richmond, 1963.

Inman, D. L., Wave-generated ripples in nearshore sands, *Tech. Memo. 100*, Beach Erosion Board, U.S. Army Corps of Eng., Washington, D. C., 1957.

Lee, T. H., Acoustic measurement and modeling of the vertical distribution of suspended sediment driven by waves and currents, Ph.D. dissertation, Coastal and Oceanogr. Eng. Dep., Univ. of Fla., Gainesville, 1994.

Lee, T. H., and D. M. Hanes, Explicit solution to the acoustic backscatter equation to measure the concentration of uniform, suspended particles, *J. Geophys. Res.*, *100*(C2), 2649–2657, 1995.

Madsen, O. S., and P. N. Wikramanayake, Simple model for turbulent wave-current bottom boundary layer flow, *Contract Rep. DRP-91-1*, Coastal Eng. Res. Cent., U.S. Army Corps of Eng., Vicksburg, Miss., 1991.

McFetridge, W. F., and P. Nielsen, Sediment suspension by nonbreaking waves over rippled beds, *Tech. Rep. UFL/COEL-85/005*, Coastal and Oceanogr. Eng. Dep., Univ. of Fla., Gainesville, 1985.

Miller, M. C., and P. D. Komar, A field investigation of the relationship between oscillation ripple spacing and the near-bottom water orbital motion, *J. Sediment. Petrol.*, *50*(1), 183–191, 1980.

Nielsen, P., Field measurements of time-averaged suspended sediment concentrations under waves, *Coastal Eng.*, *8*, 51–72, 1984.

Nielsen, P., Coastal bottom boundary layers and sediment transport, in *Port Engineering*, vol. 2, 4th ed., pp. 550–585, Gulf, Houston, Tex., 1990.

Nielsen, P., *Coastal Bottom Boundary Layers and Sediment Transport*, World Sci., River Edge, N. J., 1992.

Swart, D. H., Offshore sediment transport and equilibrium beach profiles, *Publ. 131*, Delft Hydrol. Lab., Delft, Netherlands, 1974.

Thorne, P. D., P. J. Hardcastle, and R. L. Soulsby, Analysis of acoustic measurements of suspended sediments, *J. Geophys. Res.*, *98*, 899–910, 1993.

Wikramanayake, P. N., Velocity profiles and suspended sediment transport, Ph.D. dissertation, Dep. of Civ. and Environ. Eng., Mass. Inst. of Technol., Cambridge, 1993.

D. M. Hanes, Coastal and Oceanographic Engineering Department, University of Florida, 336 Weil Hall, Gainesville, FL 32611. (e-mail: hanes@coed.coastal.ufl.edu)

T. H. Lee, Daewoo Corporation, C. P. O. Box 8629, Seoul 100-095, Korea.

(Received October 20, 1994; revised July 5, 1995; accepted October 2, 1995.)